

Multi-wavelength Study of A Superflare on RS CVn-type Star HD 22468 Triggered at Hard X-ray by SVOM

J. WANG,¹ W. J. XIE,¹ F. CANGEMI,² A. COLEIRO,² H. L. LI,¹ Y. XU,¹ X. H. HAN,¹ H. YANG,³ L. P. XIN,¹ X. MAO,^{1,4} J. ZHENG,¹ J. J. JIN,¹ G. W. LI,¹ J. RODRIGUEZ,⁵ L. TAO,⁶ B. CORDIER,⁷ J. Y. WEI,^{1,4}

P. BACON,² N. BELLEMONT,² L. BOUCHET,³ H. B. CAI,¹ C. CAVET,² Z. G. DAI,⁸ O. GODET,³ A. GOLDWURM,^{9,10} S. GUILLOT,³ L. HUANG,¹ M. H. HUANG,¹ N. JIANG,⁸ E. W. LIANG,¹¹ X. M. LU,¹ S. SCHANNE,⁵ S. LE STUM,² Y. L. QIU,¹ X. G. WANG,¹¹ X. Y. WANG,¹² C. WU,¹ L. ZHANG⁶ AND S. N. ZHANG⁶

¹National Astronomical Observatories, Chinese Academy of Sciences, Beijing 100101, People's Republic of China

²Universite Paris Cite, CNRS, Astroparticule et Cosmologie, F-75013 Paris, France

³Institute de Recherche en Astrophysique & Planetologie, 9 avenue du colonel Roche, 31028 Toulouse Cedex 04, France

⁴School of Astronomy and Space Science, University of Chinese Academy of Sciences, Beijing, People's Republic of China

⁵Universite Paris-Saclay, Universite Paris Cite, CEA, CNRS, AIM, 91191 Gif-sur-Yvette, France

⁶Institute of High Energy Physics, Chinese Academy of Sciences, 100049 Beijing

⁷Universitee Paris-Saclay, Universitee Paris Cite, CEA, CNRS, AIM, 91191 Gif-sur-Yvette, France

⁸Department of Astronomy, University of Science and Technology of China, Hefei 230026, China

⁹Universite Paris Cite, CNRS, CEA, Astroparticule et Cosmologie, F-75013 Paris, France

¹⁰CEA Paris-Saclay, Irfu / Departement d'Astrophysique, F-91191 Gif-sur-Yvette, France

¹¹Guangxi Key Laboratory for Relativistic Astrophysics, School of Physical Science and Technology, Guangxi University, Nanning 530004, People's Republic of China

¹²School of Astronomy and Space Science, Nanjing University, Nanjing 210023, Jiangsu, People's Republic of China

ABSTRACT

Detection of stellar flares at hard X-ray is still rare at the current stage. A transient was recently detected by the hard X-ray camera, ECLAIRs onboard the SVOM mission at 11:39:01.2UT on 2025, January 09. Simultaneous monitor in the optical band on the ground by SVOM/GWAC and follow-up spectroscopy enable us to confirm that the transient is caused by a superflare on HD 22468, a RS CVn-type star. The bolometric energy released in the flare is estimated to be $\sim 7.2 \times 10^{37} - 1.7 \times 10^{38}$ erg. The hard X-ray spectra of the event at the peak can be reproduced by the “apec” model of a hot plasma with a temperature of 106^{+27}_{-22} MK. In the optical range, the H α emission-line profile obtained at ~ 1.7 hrs after the trigger shows a bulk blueshift of -96 ± 20 km s $^{-1}$, which can be explained by either a chromospheric evaporation or a prominence eruption. The ejected mass is estimated to be 3.9×10^{20} g for the evaporating plasma, and to be 3.2×10^{21} g $< M_p < 8.8 \times 10^{21}$ g for the erupted prominence.

Keywords: stars: flare — stars: coronae — stars: chromospheres — X-rays: stars

1. INTRODUCTION

Stellar flares, which release massive energy of 10^{33-39} erg in a very short period of time, have been detected in multiple wavelengths, from radio to X-ray, in main-sequence stars with a type from G to M, pre-main-sequence stars and RS CVn systems (e.g., Petersen 1989; Schmitt 1994; Osten et al. 2004, 2005;

Huenemoerder et al. 2010; Maehara et al. 2012; Kowalski et al. 2013; Balona 2015; Davenport et al. 2016; Notsu et al. 2016; Van Doorsselaere et al. 2017; Chang et al. 2018; Paudel et al. 2018; Schmidt et al. 2019; Xin et al. 2021, 2024; Li et al. 2023b, Li et al. 2023a, 2024; Bai et al. 2023; Wang et al. 2024; Mao et al. 2025). The RS CVn systems are close binary systems, which are usually composed of a (sub)giant and a dwarf or a subgiant. There is accumulating evidence supporting that the activity of host star is likely of decisive impact on the habitability of an exoplanet (e.g., Tian et al. 2011;

Airapetian et al. 2016, 2017; Cherenkov et al. 2017; Garcia-Sage et al. 2017; Chen et al. 2021).

By analogy with the Sun, it is commonly accepted that the flares are generated by magnetic reconnection (e.g., Noyes et al. 1984; Wright et al. 2011; Shulyak et al. 2017), although the strong magnetic fields might have diverse origins. The $\alpha\Omega$ dynamo is adopted to generate strong magnetic fields in G-type stars (e.g., Shibata & Yokoyama 2002; Getman et al. 2023), and the α^2 dynamo in cool stars because of a lack of the boundary between the radiative and convective zones (e.g., Hotta et al. 2022; Bhatia et al. 2023). Being different from the dynamos, the strong magnetic fields result from the tidal force between the binary stars in the RS CVn systems. Simon et al. (1980) proposed a scenario of a magnetic reconnection coupling the flux tubes of the two stars for the flares on the RS CVn systems.

Many details and open issues still need to be revealed and answered for the stellar flares. On the one hand, unlike in the soft X-ray ($< 10\text{keV}$) band, the hard X-ray ($\gg 10\text{keV}$) emission is still rarely detected in the flares of remote stars, partially because of the limited sensitivity of the hard X-ray survey facilities. Two superflares on II Peg and EV Lac detected by *Swift*/BAT have been reported and studied in Osten et al. (2007) and Osten et al. (2010), respectively. Tsuboi et al. (2016) reported 23 superflares on 13 active stars detected in the 2-30 keV range by the first two years survey of Monitor of All-sky X-ray Image (MAXI). By analyzing the archived data of the Nuclear spectroscopic Telescope Array (NuSTAR), NuSTAR J230059+5857.4 is identified as a stellar superflare resulting from a plasma with a temperature of 95 MK (Hakamata et al. 2025).

On the other hand, the insufficient spatial resolution of contemporary instruments results in a difficulty in detecting complicated dynamics, e.g., coronal mass ejection (CME) and chromospheric evaporation, caused by magnetic reconnection in distant stars (see Leitzinger & Odert (2022) and references therein for a recent review). A batch of candidates of CME or chromospheric evaporation (or prominence eruption) has been recently identified based on either asymmetry or bulk velocity shift of the H α and O VII $\lambda 18.97\text{\AA}$ emission lines (e.g., Moschou et al. 2019; Argiroffi et al. 2019; Cao & Gu 2024; Wang et al. 2021, 2022, 2024; Wu et al. 2022; Chen et al. 2022; Namekata et al. 2021, 2024). A filament eruption has recently been identified in the RS CVn-type star UX AI by the blueshifted H α absorption with a bulk velocity of $\sim 140 \text{ km s}^{-1}$ (Cao & Gu 2025).

In this paper, we report the discovery and a follow-up observation in time-resolved spectroscopy for the hard X-ray transient SVOM J00365+0033 triggered by

SVOM/ECLAIRs, which allows us to identify that the transient is caused by a flare from a RS CVn-type star. SVOM, launched on 2024 June 22, is a Chinese-French space mission dedicated to the detection and study of gamma-ray bursts and high-energy transients. We refer the reader to Atteia et al. (2022) and the white paper given by Wei et al. (2016) for details. The follow-up spectroscopy reveals a low-speed outflow possibly related to a chromospheric evaporation or a prominence eruption associated with the flare.

The paper is organized as follows. Section 2 presents the hard X-ray transient triggered by the SVOM/ECLAIRs. A simultaneous monitor by SVOM/GWAC on the ground is described in Section 3. Our follow-up observations in spectroscopy, along with data reduction, are given in Section 4. Section 5 shows the analysis and results. The implications are presented in Section 6.

2. HARD X-RAY TRANSIENT DETECTED BY SVOM/ECLAIRS

The hard X-ray transient SVOM J00365+0033 (ID=sb25010902) triggered the soft γ -ray Camera ECLAIRs on board SVOM at 2025-01-09UT11:39:01.2 (MJD = 60684.98543, hereafter t_0).

ECLAIRs is the wide-field ($\text{FoV} \sim 2 \text{ sr}$) coded-mask ($\sim 40\%$ transparency below 80 keV) trigger camera of SVOM (e.g., Schanne et al. 2013; Le Provost et al. 2013; Godet et al. 2014; Lacombe et al. 2014; Xie et al. 2024; Llamas Lanza et al. 2024). It works in the energy range of 4-120 keV, and has an active area $\approx 1000 \text{ cm}^2$ in the detection plane. The localization accuracy is $13'$ at a 90% confidence level for on-axis weak sources with a signal-to-noise ratio (S/N) ~ 10 , and better than $2'$ for bright sources with $S/N \sim 100$ (Goldwurm et al. 2026, in preparation).

Figure 1 shows the discovery sky image of the transient taken by ECLAIRs. The transient with an S/N of 9.47 was located at R.A. = $03^{\text{h}}36^{\text{m}}39^{\text{s}}$ and Dec = $00^{\circ}33'25''$ with an uncertainty of $8'.4$ (radius, 90% confidence level including both statistical and systematic errors) based on Eq.(10) in Goldwurm & Gros (2022).

At a distance of $4'$ away from the center determined by ECLAIRs, there exists a bright X-ray source listed in the ROSAT All-sky Bright Source Catalog (Voges et al. 1999), enhanced 3XMM catalog (Rosen et al. 2016), and Chandra source catalog (Evans et al. 2010). The X-ray source (1RXS J033647.2+003518 = 3XMM J033647.2+003515) has a flux of $7.9 \times 10^{-11} \text{ erg s}^{-1} \text{ cm}^{-2}$ in the 0.2-12 keV band (Rosen et al. 2016), and shows X-ray flares detected by XMM-

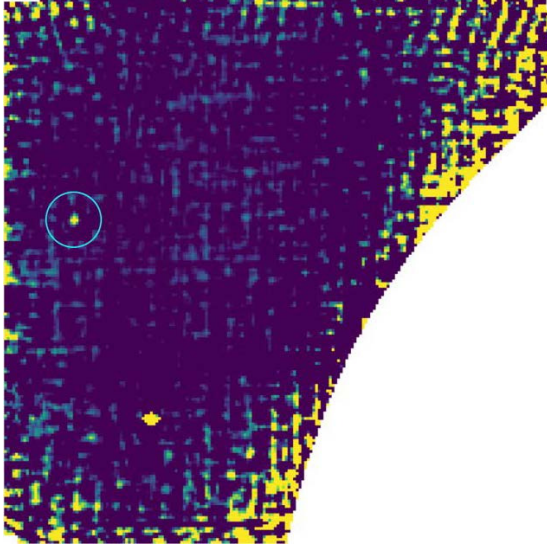


Figure 1. The discovery image of SVOM J00365+0033 (ID=sb25010902) taken by SVOM/ECLAIRs. The source is marked by the blue circle. The bright source at the bottom right of SVOM J00365+0033 is the Crab. The blank at the right-bottom corner is due to the obscuration of the Earth.

Newton serendipitous observations as reported in Pye et al. (2015). This X-ray source is associated with a RS CVn-type star HD 22468 (=HR 1099) that is well known for its plentiful flares from radio to X-ray (e.g., Foing et al. 1994; Osten et al. 2004; Pandey & Singh 2012; Didel et al. 2025). Combining these facts and the evolution in X-ray, optical continuum and H α emission line (see below) enable us to identify the event SVOM J00365+0033 as resulting from a stellar flare occurring on HD 22468. The basic properties of HD 22468 are listed in Table 1.

Even though the high S/N ratio of 9.47 of the event was reached, a follow-up snapshot by both the narrow-field instruments, MXT and VT, onboard SVOM was not performed because an automatic slew of the platform has been rejected due to an ongoing Target-of-Opportunity observation with a higher priority. The star is actually too bright to be observed by VT. A star with a brightness of 8th magnitude is in fact saturated in the VT image for the shortest exposure of 1 second.

3. SIMULTANEOUS MONITOR BY SVOM/GWAC AND DATA REDUCTION

During the night of 2025, January 09, the sky area covered by the ECLAIRs was simultaneously monitored by the SVOM/GWAC (Ground-based Wide Angle Cameras) deployed in Xinglong Observatory, Chinese Academy of Sciences, since the observation plan of SVOM/GWAC is designed to monitor the sky region covered by ECLAIRs as much as possible (see Han et

Table 1. Properties of HD 22468

Property (1)	Value (2)
R.A.	03 ^h : 36 ^m : 47 ^s .3
Dec	+00°:35':16''
Sp. T	K1IV+G5V
Distance (pc)	29.43 ± 0.03
M_G (mag)	2.9
P_{rot} (day)	2.84
$V \sin i$ (km s ⁻¹)	34.5
Primary	
G-band (mag)	5.62
GBp-GRp (mag)	1.22
M_{\star} (M_{\odot})	1.5
R_{\star} (R_{\odot})	4.0
T_{eff} (K)	4712 ± 38
$\log(g/\text{cm s}^{-2})$	3.4 ± 0.1
[Fe/H]	-0.16 ± 0.05
Secondary	
G-band (mag)	8.52
GBp-GRp (mag)	1.19
M_{\star} (M_{\odot})	0.6
T_{eff} (K)	4631 ± 50
$\log(g/\text{cm s}^{-2})$	4.5 ± 0.1

NOTE—References: Gaia Collaboration et al. (2022); Kervella et al. (2022); Soubiran et al. (2022); Seli et al. (2022), Luck et al. (2017)

al. 2021, Li et al. 2024 for a description of GWAC in details).

Up to the beginning of 2025, SVOM/GWAC was in total composed of 10 mounts. Each mount has four Joint Field-of-View (JFoV) cameras and one Full Field-of-View (FFoV) cameras. The diameters of the JFoV and FFoV cameras are 18 cm and 3.5 cm, respectively. The FFoV is used to guide the pointing of the mount, and to monitor the bright sources that are saturated in the JFoV images. A 4K × 4K Dhyana 4040BSI CMOS detector is equipped on each JFoV camera, and the ZWO ASI2600MCAir CMOS¹ detector, with a size of 6248 × 4176 pixels, on each FFoV camera. The field-of-view (FoV) is 9°.8 × 9°.8 for each JFoV camera, and 64° × 42° for each FFoV camera. The total FoV of the 40 JFoV cameras is ∼ 3600 deg². The exposure time of each camera is fixed to be 3 s, and the readout time is 1 s, which result in a cadence of 4 s.

The sky field around the event of SVOM J00365+0033 was monitored by the GWAC mount #2 from MJD 60684.92381 to 60685.095429, i.e., ≈ 4.11 hr duration.

¹ <https://www.zwoastro.com/product/asi2600/>

The host star HD 22468 was in fact saturated in the JFoV images, but not in the images taken by the FFoV camera. The FFoV images were reduced by the standard procedure, including bias, dark, and flat-field corrections, by using the IRAF² package. An aperture photometry was then performed by adopting an aperture size of 3 pixels. Finally, the USNO B1.0 catalog (Monet et al. 2003) was used to carry out absolute photometric calibration. The limiting magnitude of FFoV is determined to be 11.8 mag during the monitor.

4. SPECTROSCOPIC FOLLOW-UP OBSERVATIONS AND DATA REDUCTIONS

Spectroscopy of HD 22468 has been taken with the NAOC 2.16 m telescope (Fan et al. 2016) in three observational runs after the ECLAIRs trigger. The log of the spectroscopic observations is tabulated in Table 2, where the Column (1) lists the start time of each observational run. Our first spectrum was obtained ≈ 1.7 hr after the trigger.

All spectra were taken with the Beijing Faint Object Spectrograph and Camera that is equipped with a back-illuminated E2V55-30 AIMO CCD. A total of 10 frames were obtained in each observational run, in which the exposure time of each frame is 30 seconds. The G8 grism with a wavelength coverage of 5800 to 8200 \AA was used in the observations, which allows us to study the H α emission-line profile with adequate spectral resolution. With a slit width of 1''.8 oriented in the south–north direction, the resolution is measured to be 3.5 \AA according to the sky emission lines, which corresponds to $R = \lambda/\Delta\lambda = 1880$ and a velocity of 160 km s $^{-1}$ for the H α emission line. The wavelength calibration was carried out with iron–argon comparison lamps. Flux calibration was carried out by the observations of the standard stars from the Kitt Peak National Observatory (Massey et al. 1988).

The one-dimensional (1D) spectrum was extracted from each of the raw images by using the IRAF package and standard procedures, including bias subtraction and flat-field correction. In the spectral extraction, the apertures of both source and sky emission were fixed for both object and corresponding standard. The extracted 1D spectra were then calibrated in wavelength and in flux by the corresponding comparison lamps and standard stars, respectively. The zero-point of the wavelength calibration was corrected for each spectrum by using the sky

[O I] λ 6300 emission line as a reference. The accuracy of wavelength calibration is therefore determined to be $\sim 0.1\text{\AA}$, which corresponds to a velocity of ~ 5 km s $^{-1}$ for the H α line.

5. ANALYSIS AND RESULTS

5.1. Hard X-ray Spectra and Light Curves

After taking into account the obscuration by the Earth, the hard X-ray spectra of SVOM J00365+0033 are extracted in four epochs, i.e., $[t_0 - 4000, t_0 - 3000]$ s, $[t_0, t_0 + 940]$ s, $[t_0 + 1444, t_0 + 3500]$ s and $[t_0 + 7273, t_0 + 9300]$ s, by the dedicated pipelines of ECLAIRs³ and the corresponding calibration files, where t_0 refers to the trigger time.

To investigate the evolution of its hard X-ray emission, we model the four time-integrated hard X-ray spectra by using the Xspec software (version 12.14.1, Arnaud 1996). The `apec` model (e.g., Smith et al. 2001) are adopted to reproduce the observed spectra. The abundance is fixed to be $0.69Z_\odot$ in the modeling⁴. The best fits are illustrated in Figure 2 for the three epochs after the trigger, and the corresponding results are tabulated in Table 3. All the errors reported in the table are obtained by using the `error` command in the Xspec package, and are at the 90% significance level.

In the second epoch, the spectrum can be reproduced by a hot plasma with a temperature of 106^{+27}_{-22} MK when the `apec` model is adopted (see the upper-left panel in Figure 2). This temperature is actually comparable to the measurement in the stellar flare event NuSTAR J230059+5857.4 (Hakamata et al. 2025).

After the modeling of the energy spectra, the evolution of the modeled X-ray flux in the 4–120 keV band and the plasma temperature are displayed in the upper two panels of Figure 3. In the top panel, the quiescent flux level in the 4–120 keV band, i.e., $F_{\text{X,q}} = 5.6 \times 10^{-13} - 1.7 \times 10^{-11}$ erg s $^{-1}$ cm $^{-2}$, is converted from the flux listed in the 3XMM catalog by using the `pimms` task, in which the `apec` model is considered. The plasma temperature ranges from $kT = 1$ keV to 3 keV in the conversion. The ECLAIRs detection thresholds⁵ at a 3σ significance level are calculated by adopting the same models, and marked in the plot by the light-blue region.

As shown in the plot, the event was marginally detected before the trigger time. After the trigger time, the light curves are typical of a stellar flare in which the

³ <https://fsc.svom.org/documentation/ecpi/index.html>

⁴ The abundance is inferred from the [Fe/H] value by assuming the solar composition.

⁵ The threshold at a 3σ significance level is estimated to have a count rate of 0.07 count s $^{-1}$ for an 1 000 seconds exposure.

² IRAF is distributed by the National Optical Astronomical Observatories, which are operated by the Association of Universities for Research in Astronomy, Inc., under cooperative agreement with the National Science Foundation.

Table 2. Observational Log and Results of Optical Spectroscopic Analysis.

UT (1)	Exp time second (2)	f_c erg s $^{-1}$ cm $^{-2}$ Å $^{-1}$ (3)	EW(FeIλ6495) Å (4)	$f_{H\alpha}$ erg s $^{-1}$ cm $^{-2}$ (5)	$\Delta v(H\alpha)$ km s $^{-1}$ (6)
2025-01-09T13:22:55	10 × 30	1.6×10^{-11}	1.10 ± 0.09	$(2.4 \pm 0.1) \times 10^{-11}$	-96 ± 20
2025-01-10T11:11:45	10 × 30	1.4×10^{-11}	0.97 ± 0.07	$(1.8 \pm 0.1) \times 10^{-11}$	-50 ± 16
2025-02-05T10:55:35	10 × 30	1.3×10^{-11}	0.99 ± 0.08	$(1.1 \pm 0.1) \times 10^{-11}$	-14 ± 17

NOTE—Column (1): the start time of spectroscopy in UT. Column (2): the total exposure time in unit of second. Column (3): the continuum flux density measured in the wavelength range between 6515Å and 6545Å. Column (4): the equivalent width of Fe Iλ6496 absorption feature. Column (5): the flux of H α emission line. Column (6): the bulk velocity shift of H α line measured with respect to the stellar photosphere.

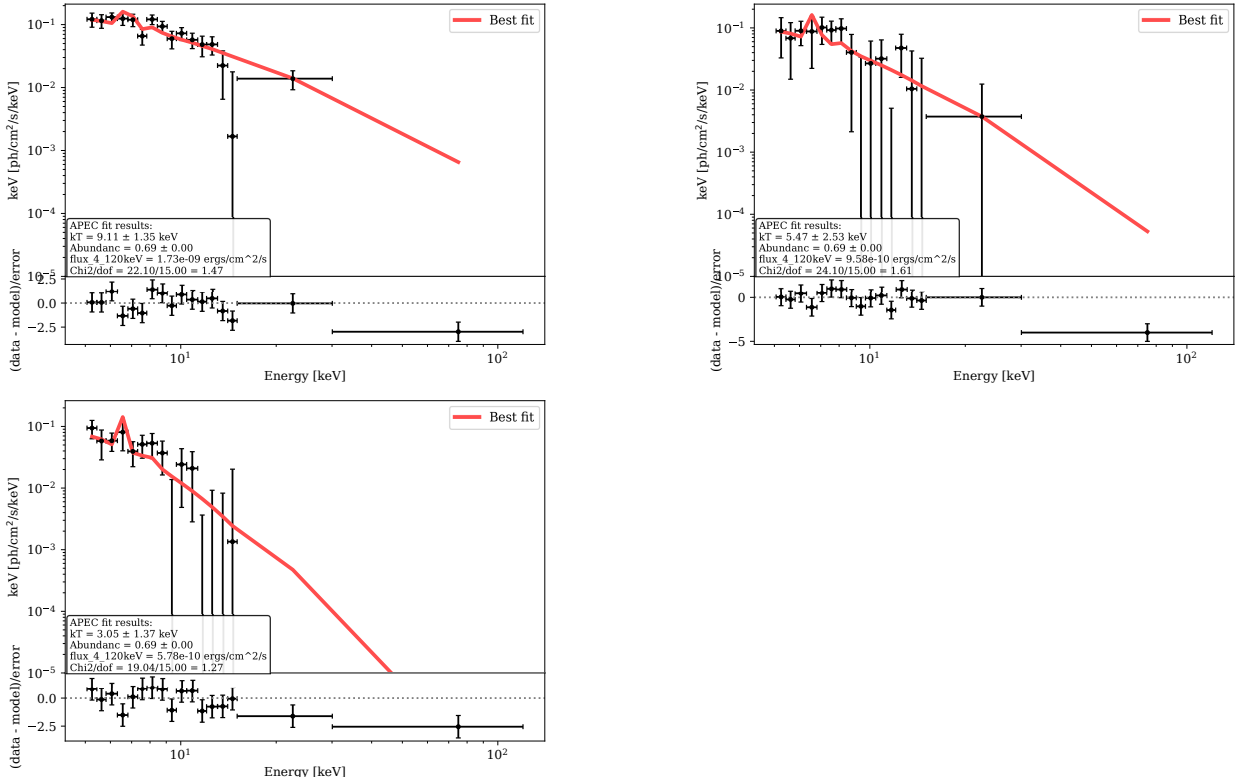


Figure 2. *Upper-left panel:* Hard X-ray spectrum of SVOM J00365+0033 observed by SVOM/ECLAIRs in the epoch of $[t_0, t_0 + 940]$ s, where t_0 is the trigger time. The best-fit apec model is overplotted by the red line. A fixed abundance of $0.69Z_\odot$ is adopted in the modeling. The subpanel underneath the spectrum shows the residuals, in units of counts s $^{-1}$ keV $^{-1}$, of the observed data from the best-fit model. *Upper-right and lower-left panels:* the same as the left one, but for the epochs of $[t_0 + 1444, t_0 + 3500]$ s and $[t_0 + 7273, t_0 + 9300]$ s, respectively.

hard X-ray emission quickly fades out along with a fast cooling of the plasma (e.g., Mao et al. 2025). We model the hard X-ray light curve by

$$F(t) = (F_p - F_q) \times \exp\left(-\frac{t - t_p}{\tau}\right) + F_q, \quad t > t_p \quad (1)$$

where F_p and t_p are the peak flux and time, respectively. F_q is the corresponding quiescent flux. By setting $t_p = t_0$, the fitting yields $F_p = (1.7 \pm 0.3) \times 10^{-9}$ erg s $^{-1}$ cm $^{-2}$

and $\tau = 108.8 \pm 47.8$ min. The best fit is overplotted in Figure 3 by the solid line. Based on the fitting, the total energy released in the 4 – 120 keV is roughly estimated to be $E_{4-120\text{keV}} = (1.2 \pm 0.5) \times 10^{36}$ erg for SVOM J00365+0033, which corresponds to a value of $E_X \sim 1.7 \times 10^{36}$ erg in the 0.2 – 12 keV band by using the pimms task⁶. The bolometric energy released in the

⁶ The plasma temperature is fixed to be $kT = 9.2$ keV.

Table 3. X-Ray Spectral Fit Parameters of SVOM J00365+0033

$t - t_0$ second	kT keV	Norm	$F_{4-120\text{keV}}$ erg cm $^{-2}$ s $^{-1}$	$\chi^2/\text{d.o.f}$
(1)	(2)	(3)	(4)	(5)
(-4000, -3000)	$7.8^{+9.42}_{-4.92}$	$0.66^{+1.21}_{-0.29}$	$8.0^{+4.4}_{-1.4} \times 10^{-10}$	1.08
(0, 940)	$9.2^{+2.3}_{-1.9}$	$1.2^{+0.2}_{-0.2}$	$1.7^{+0.1}_{-0.2} \times 10^{-9}$	1.47
(1444, 3500)	$4.7^{+2.6}_{-1.9}$	$1.3^{+1.4}_{-0.5}$	$9.2^{+0.6}_{-3.1} \times 10^{-10}$	1.61
(7273, 9300)	$3.0^{+2.5}_{-1.6}$	$1.6^{+6.8}_{-0.9}$	$5.8^{+0.2}_{-4.2} \times 10^{-10}$	1.27

NOTE—Column (1): The time window in which the X-ray spectra are extracted and modeled, where t_0 is the trigger time of ECLAIRs. Column (2-4): The best-fit temperature, normalization and flux in 4 – 120 keV when the `apec` model is adopted. The reported uncertainties correspond to a 90% significance level. Column (5): The final reduced χ^2 .

flare is then estimated to be $E_{\text{bol}} \sim 1.7 \times 10^{38}$ erg, when a bolometric correction $E_{\text{X}}/E_{\text{bol}} = 0.01$ is adopted (e.g., Emslie et al. 2012; Wang 2023).

The emission measurement (EM) is calculated to be $\text{EM} = \int n_e^2 dV = 4 \times 10^{14} \pi d^2 \times \text{norm} = (1.3 \pm 0.2) \times 10^{55} \text{ cm}^{-3}$, where n_e is the electron density, V the emitting volume, and d the distance to the star in unit of cm. The norm is one of the parameters in the `apec` model.

5.2. Light Curve in White-light

After binning with a bin size of 10 minutes, the light curve derived from the GWAC images is presented in the bottom panel in Figure 3 for HD 22468. A white-light (WL) flare peaking at ~ 1 hour after the ECLAIRs trigger can be identified for a brightening of ~ 0.05 mag at a significance level of $\sim 3\sigma$, which supports the claim that SVOM J00365+0033 originated from stellar activity on HD 22468.

The flaring energy released in the R -band is estimated to be $E_R \sim 1.2 \times 10^{37}$ erg by an integration of the light curve. This value yields a bolometric energy of $E_{\text{bol}} \sim 7.2 \times 10^{37}$ erg when a bolometric correction of $E_{\text{bol}}/E_R = 6$ derived from a blackbody with a temperature of 10 4 K is adopted. The effect of reddening caused by the Galaxy is ignored in the calculation due to the extremely small color excess $E(B - V) \approx 0.02$ mag. By assuming the hydrogen density around the Sun of $n_H = 10^6 \text{ cm}^{-3}$ and the constant dust-to-gas ratio, this color excess is estimated from the calibration of $E(B - V) \approx 0.53 \times (d/\text{kpc})$ (Bohlin et al. 1978), where d is the distance of the object.

5.3. Decay and Blueshift of H α Emission Line

After combining the individual spectra taken in each run, the three combined spectra taken at the three different epochs are compared in the upper panel of Figure

4. In addition to the Fe I $\lambda 6496$ absorption feature arising from the photosphere, a decrease can be observed in both continuum and H α emission line from the chromosphere.

After normalizing the continuum by a spline function, each of the features of Fe I $\lambda 6496$ and H α is modeled by a Gaussian function by the IRAF/SPECFIT task (Kriss 1994). The modeling is illustrated in the three lower panels in Figure 4. The results of the modeling are tabulated in Table 2, where all the uncertainties correspond to the 1σ significance level resulted from the modeling. f_c listed in Column (3) is the continuum flux level directly measured in the wavelength range from 6515 \AA to 6545 \AA by the `splot` task in the IRAF package. The continuum slightly decreases from $1.6 \times 10^{-11} \text{ erg s}^{-1} \text{ cm}^{-2} \text{ \AA}^{-1}$ to the quiescent level of $1.3 \times 10^{-11} \text{ erg s}^{-1} \text{ cm}^{-2} \text{ \AA}^{-1}$, which corresponds to a differential magnitude of ~ 0.2 mag. In addition to the decay of the continuum, the H α line emission decreases by a factor of two from the active to the quiescent states. The decay of both continuum and H α line emission reinforces our identification that SVOM J00365+0033 is resulting from stellar activity on RS CVn-type star HD 22468.

Column (6) in Table 2 lists the bulk velocity shift of the H α emission $\Delta v_{\text{H}\alpha}$. It is calculated as

$$\Delta v_{\text{H}\alpha} = c \times \frac{\Delta\lambda - \Delta\lambda^0}{\lambda_{\text{H}\alpha}^0} \quad (2)$$

where $\Delta\lambda = \lambda_{\text{H}\alpha} - \lambda_{\text{FeI}}$ and $\Delta\lambda^0 = \lambda_{\text{H}\alpha}^0 - \lambda_{\text{FeI}}^0$. $\lambda_{\text{H}\alpha}^0$ ($\lambda_{\text{H}\alpha}$) and λ_{FeI}^0 (λ_{FeI}) are the (observed) wavelengths measured in laboratory of the H α and Fe I $\lambda 6495$ lines, respectively. According to this definition, a positive $\Delta v_{\text{H}\alpha}$ denotes a downflow, and a negative one an upflow.

We argue that the large H α off-set velocity of $\sim -100 \text{ km s}^{-1}$ revealed in the spectrum taken at ~ 1.7 hrs after the trigger of ECLAIRs is most likely resulted from an upward plasma motion related with the flare. On the one hand, since the absorption Fe I feature certainly comes from the underlying photosphere, the velocity $\Delta v_{\text{H}\alpha}$ is therefore unaffected by the orbiting of the binary, and reflects a plasma motion with respect to photosphere. On the other hand, the contribution from chromospheric active region associated with stellar rotation is too small to explain the measured large H α off-set velocity. In fact, the rotational velocities have been measured to be $\sim 41 \text{ km s}^{-1}$ and $\sim 8 \text{ km s}^{-1}$ for the cool and hot stars, respectively (De Medeiros et al. 2004; Gleboki & Gnacinski 2005; Herrero et al. 2012; Luck 2017).

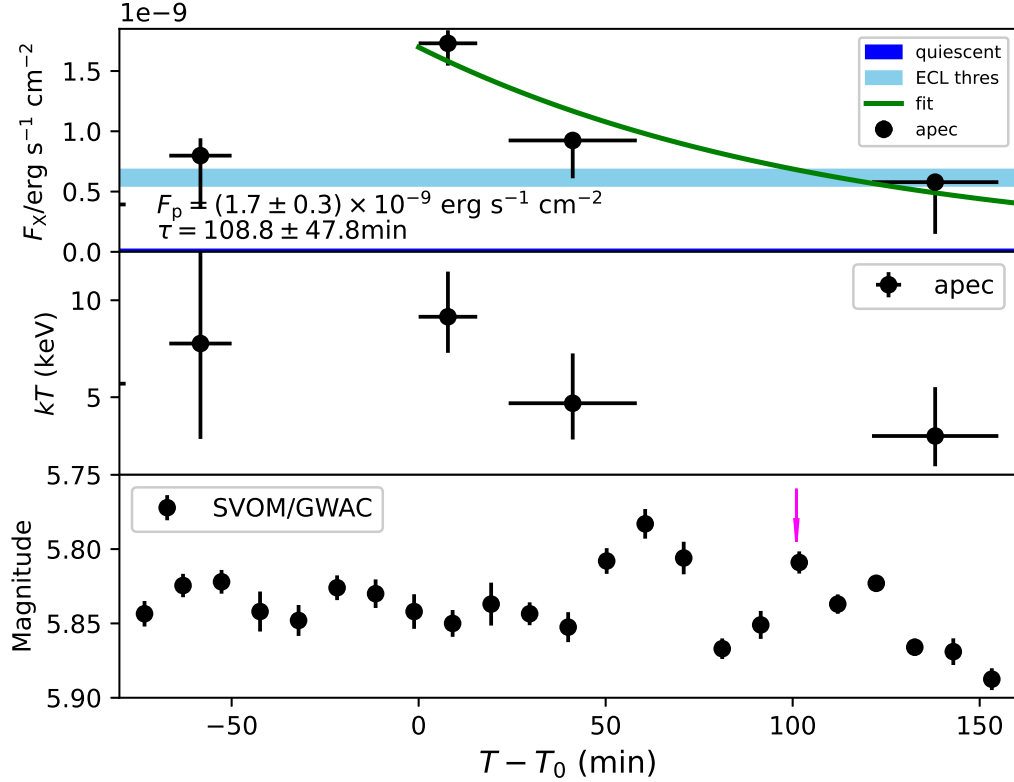


Figure 3. *Top panel:* the hard X-ray light curve of SVOM J00365+0033 detected by SVOM/ECLAIRs in 4 – 120 keV band. The dark-blue shadow region at the bottom of the panel marks the quiescent emission level estimated from the 3XMM catalog (see main text for the details). The sky-blue region corresponds to the 3σ ECLAIRs detection thresholds for a 1 000 seconds exposure. T_0 is the ECLAIRs trigger time. *Middle panel:* evolution of the modeled plasma temperature. *Bottom panel:* the white-light light curve of HD 22468 monitored by the SVOM/GWAC FFoV camera in 2025, January 09, after binning the data by averaging the measurements within every 10 minutes. The epoch of our first spectroscopic follow-up is marked by the downward magenta arrow.

6. DISCUSSION

A multi-wavelength study is performed on the transient event SVOM J00365+0033 triggered by SVOM/ECLAIRs in 2025, January 09, which enables us to identify the event is originated from a flare from RS CVn-type star HD 22468. The star was revealed to have both a WL flare and enhanced $\text{H}\alpha$ emission seen in optical band at 1 – 2 hours after the trigger. The bolometric energy released in the flare is estimated to be $\sim 7.2 \times 10^{37}$ erg and $\sim 1.7 \times 10^{38}$ erg from the WL and X-ray light curves, respectively. In addition, an upflow with a velocity of $-96 \pm 20 \text{ km s}^{-1}$ with respect to the photosphere is revealed from the $\text{H}\alpha$ emission line.

6.1. Discrepancy in the Bolometric Energy

Although an estimation of bolometric energy strongly depends on the adopted bolometric correction, the above discrepancy between the bolometric energy obtained from the light curves in the two different bands is likely

resulted from the different integration ways. Not as a modeling by an exponential decay in the X-ray band, an over simplified integration is adopted for the WL light curve, which result in an underestimation of the total released energy as follows. Because of the small flaring amplitude in WL, the WL light curve is integrated by simply adding all the points exceeding the 1σ fluctuation determined in the quiescent state before the flare. The relatively large fluctuation naturally leads to an neglecting of the late gradual decaying phase in the integration. The gradual decaying phase has non-negligible contribution to the total released energy since its long duration, even though at a low emission level.

6.2. Flare Properties

The event SVOM J00365+0033 is marked on the EM– T diagram (Shibata & Yokoyama 2002) in Figure 5, in which the event falls within the upper-right area occupied by the RS CVn-type stars.

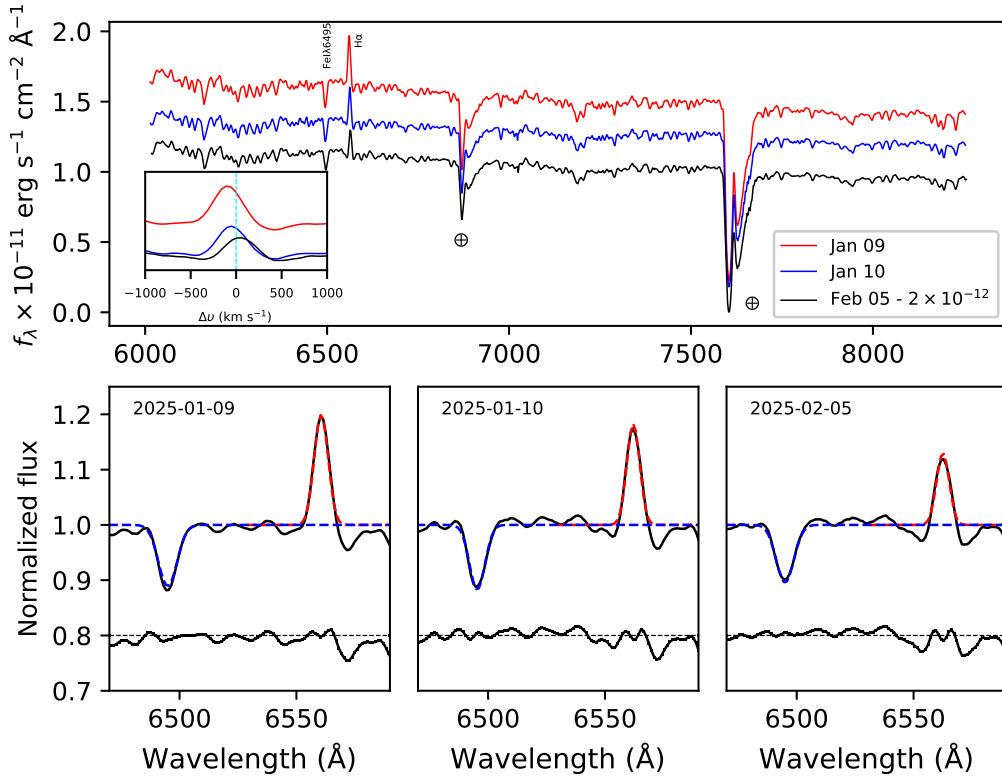


Figure 4. *Upper panel:* a comparison of the spectra of HD 22468 taken in the three different epochs. Note that the spectrum in the quiescent state (black line) obtained in 2025, February 05 is shifted vertically by an arbitrary amount for visibility. The insert panel compares the H α line profiles obtained in the three different epochs. *Bottom panels:* the modeling of the Fe I λ 6496 absorption feature and the H α emission line in the three epochs. Each line is reproduced by a Gaussian function. In each sub-panel, the observed and modeled line profiles are plotted by the black and red (blue) solid lines, respectively. The curves underneath each line spectrum present the residuals between the observed and modeled profiles.

We estimate the loop length (L), electron density (n_e) and magnetic field (B) by following the scaling laws given in Shibata & Yokoyama (2002):

$$L_9 = f_{0.1}^{-3/5} \text{EM}_{47}^{3/5} T_7^{-8/5} n_{09}^{-2/5} \quad (3)$$

$$n_9 = 10^{1.5} f_{0.1}^{2/5} \text{EM}_{47}^{-2/5} T_7^{12/5} n_{09}^{3/5} \quad (4)$$

$$B_{50} = f_{0.1}^{1/5} \text{EM}_{47}^{-1/5} T_7^{17/10} n_{09}^{3/10} \quad (5)$$

where $L_9 = L/10^9$ cm, $n_9 = n/10^9$ cm $^{-3}$, $B_{50} = B/50$ G, $\text{EM}_{47} = \text{EM}/10^{47}$ cm $^{-3}$, $T_7 = T/10^7$ K and $n_{09} = n_0/10^9$ cm $^{-3}$. $f_{0.1} = f/0.1$ is the filling factor of the hot plasma in the flare loop. By adopting the typical value of $f_{0.1} = 1$ and $n_{09} = 1$, we find $L = 1.7 \times 10^{12}$ cm, $n_e = 5.2 \times 10^9$ cm $^{-3}$ and $B = 66$ G.

The properties estimated above are actually comparable to those of the superflares recently detected by LEIA in giant HD 251108 (Mao et al. 2025), and by NuSTAR in NuSTAR J230059+5857.4 (Hakamata et al. 2025).

6.3. Plasma Motion Driven by Magnetic Reconnection

Assuming the detected flare occurs in the primary of HD 22468⁷, the escaping velocity can be estimated to be $v_{\text{esc}} = 630(M_*/M_\odot)^{1/2}(R_*/R_\odot)^{-1/2} \approx 390$ km s $^{-1}$. Because this value is far larger than the outflow velocity determined from the modeling of the H α line profile, we suggest that the upflow revealed in this study can be interpreted by either chromospheric evaporation or prominence eruption. Both scenarios are related with the energy released in a magnetic reconnection process.

6.3.1. Chromospheric Evaporation

In the chromospheric evaporation scenario, the chromospheric plasma can be heated rapidly to a very high temperature by Coulomb collisions of the electrons ac-

⁷ The primary K-type giant in HD 22468 is believed to be more active than the secondary since the primary shows significantly stronger Mg II emission lines during previous flares (e.g., Linsky et al. 1989).

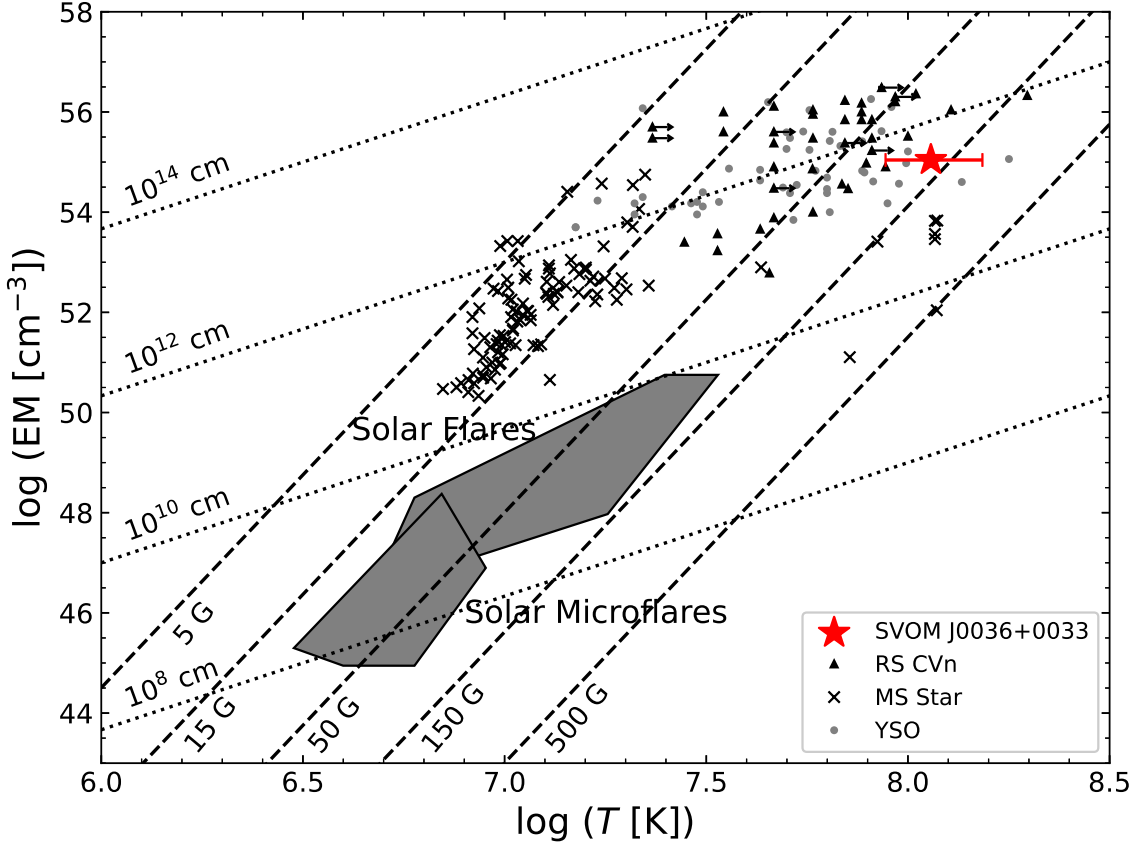


Figure 5. EM–T diagram. The event SVOM J0036+0033 is marked with the red star. The triangles show the RS CVn-type stars (Tsuru et al. 1989; Endl et al. 1997; Franciosini et al. 2001; Pandey & Singh 2012; Tsuboi et al. 2016; Sasaki et al. 2021; Karmakar et al. 2023; Mao et al. 2025), and the crosses the main-sequence stars (Pye et al. 2015). The gray dots mark the positions of young stellar objects extracted from Getman & Feigelson (2021). The filled polygons denote the solar flares (Feldman et al. 1995) and solar microflares (Shimizu 1995). The dashed lines indicate the relation of $EM \propto B^{-5} T^{17/2}$ for a constant magnetic field, and the dotted lines the relation of $EM \propto B^{5/3} T^{8/3}$ at certain loop lengths (Shibata & Yokoyama 1999).

celerated by the energy released in the magnetic reconnection (e.g., Fisher et al. 1985; Canfield et al. 1990; Gunn et al. 1994; Innes et al. 1997; Berdyugina et al. 1999; Li 2019; Tei et al. 2018; Yan et al. 2021; Fletcher et al. 2011; Tan et al. 2020; Chen et al. 2020). This heating results in an over-pressure in the chromosphere, which then pushes the plasma upward (e.g., Fisher et al. 1985; Teriaca et al. 2003; Zhang et al. 2016; Brosius & Daw 2015; Tian & Chen 2018) or downward (e.g., Kamio et al. 2005; Libbrecht et al. 2019; Graham et al. 2020). Both upward and downward motion of chromospheric plasma have been infrequently diagnosed and reported for cool main-sequence stars and RS CVn-type stars in previous studies (e.g., Honda et al. 2018; Koller et al. 2021; Wang et al. 2024; Cao & Gu 2024, 2025).

The upward velocity is typically of tens of kilometers per second in the “gentle evaporation” with an electron beaming flux $\leq 10^{10} \text{ erg s}^{-1} \text{ cm}^{-2}$ (Milligan et al. 2006; Sadykov et al. 2015; Li 2019). In addition, a fast upward

motion with a velocity of hundreds of kilometers per second can result in an electron beaming flux $\geq 3 \times 10^{10} \text{ erg cm}^{-2} \text{ s}^{-1}$ (e.g., Milligan et al. 2006b; Brosius & Inglis 2017; Li et al. 2017) in the case of a “explosive evaporation”.

In the evaporation scenario, the mass of the moving plasma can be estimated from the H α emission through the traditional method $M_{\text{gas}} \geq N_{\text{tot}} V m_{\text{H}}$ (e.g., Houdebine et al. 1990), where N_{tot} is the number density of hydrogen atoms, m_{H} the mass of the hydrogen atom, and V the total volume that can be determined from the line luminosity L_{ji} . With $L_{ji} = N_j A_{ji} h \nu_{ji} V P_{\text{esc}}$, the mass of the moving plasma M_{PL} can be estimated as

$$M_{\text{PL}} \geq \frac{4\pi d^2 f_{\text{line}} m_{\text{H}}}{A_{ji} h \nu_{ji} V P_{\text{esc}}} \frac{N_{\text{tot}}}{N_j} \quad (6)$$

where N_j is the number density of hydrogen atoms at excited level j , A_{ji} the Einstein coefficient for a sponta-

neous decay from level j to i , P_{esc} the escape probability, d the distance and f_{line} the observed line flux.

After removing the quiescent $\text{H}\alpha$ line emission and adopting $P_{\text{esc}} = 0.5$, the mass of the upward moving plasma is estimated to be as large as $M_{\text{PL}} = 3.9 \times 10^{20} \text{ g}$ by transforming the $\text{H}\alpha$ line flux to that of $\text{H}\gamma$ by assuming a Balmer decrement of three (Butler et al. 1988). $A_{52} = 2.53 \times 10^6 \text{ s}^{-1}$ (Wiese & Fuhr 2009) and $N_{\text{tot}}/N_5 = 2 \times 10^9$ are adopted in the calculation according to the non-local thermal equilibrium modeling by Houdebine & Doyle (1994a, b).

6.3.2. Prominence Eruption

Prominence eruption that has been detected in the decay phase of the flares in other stars and the Sun (e.g., Kurokawa et al. 1987) is an alternative explanation of the observed blueshifted $\text{H}\alpha$ emission (e.g., Otsu et al. 2022; Inoue et al. 2024; Wang et al. 2024).

By following the method adopted in the previous studies (e.g., Maehara et al. 2021; Inoue et al. 2023; Wang et al. 2024), we estimate the mass of the prominence by

$$M_{\text{p}} \approx 2m_{\text{H}} \left(\frac{n_{\text{H}}}{n_{\text{e}}} \right) n_{\text{e}}^{-1} \frac{d^2 f_{\text{H}\alpha}}{F_{\text{H}\alpha}} \times \text{EM} \quad (7)$$

or numerically

$$M_{\text{p}} \approx 3.2 \times 10^{19} \left(\frac{n_{\text{H}}}{n_{\text{e}}} \right) \left(\frac{n_{\text{e}}}{10^{10} \text{ cm}^{-3}} \right)^{-1} \left(\frac{d}{\text{pc}} \right)^2 \times \left(\frac{f_{\text{H}\alpha}}{10^{-10} \text{ erg s}^{-1} \text{ cm}^{-2}} \right) \left(\frac{F_{\text{H}\alpha}}{10^4 \text{ erg s}^{-1} \text{ cm}^{-2} \text{ sr}^{-1}} \right)^{-1} \times \left(\frac{\text{EM}}{10^{30} \text{ cm}^{-5}} \right) \quad (8)$$

where m_{H} is the mass of the hydrogen atom, n_{H} and n_{e} are the densities of hydrogen atom and electron, respectively. d is the distance, and $f_{\text{H}\alpha}$ the measured $\text{H}\alpha$ line flux, $\text{EM} = n_{\text{e}}^2 L$ is the emission measurement. $F_{\text{H}\alpha}$ is the prominence $\text{H}\alpha$ emission in unit of $\text{erg s}^{-1} \text{ cm}^{-2} \text{ sr}^{-1}$, and depends on the optical depth. As reported in Inoue et al. (2023), the optical depth of the prominence $\text{H}\alpha$ emission is assumed to be $0.1 < \tau < 100$. The NLTE solar prominence model (Heinzel et al. 1994) gives $F_{\text{H}\alpha} \sim 10^4 \text{ erg s}^{-1} \text{ cm}^{-2} \text{ sr}^{-1}$ and $\text{EM} \sim 10^{28} \text{ cm}^{-5}$ in the case of $\tau = 0.1$. In the case of $\tau = 100$, the corresponding values are $F_{\text{H}\alpha} \sim 10^6 \text{ erg s}^{-1} \text{ cm}^{-2} \text{ sr}^{-1}$ and $\text{EM} \sim 10^{31} \text{ cm}^{-5}$.

The properties of the flare estimated in Section 6.2 yields $\text{EM} = n_{\text{e}} L = 4.6 \times 10^{31} \text{ cm}^{-5}$, which favors the optical thick case, and results in $M_{\text{p}} \approx 1.5 \times 10^{21} (n_{\text{H}}/n_{\text{e}})$. Taking into account the $n_{\text{H}}/n_{\text{e}}$ ratio ranging from 2.13

to 5.88 for a prominence (Notsu et al. 2024), the prominence mass is estimated to be $3.2 \times 10^{21} \text{ g} < M_{\text{p}} < 8.8 \times 10^{21} \text{ g}$ for the transient SVOM J00365+0033.

6.4. The Nature of the WL Flare

Taking into account their special spectroscopic features and physical properties, three types of scenario have been proposed to understand the transporting of energy released in magnetic reconnection down to the lower chromosphere and photosphere in RS CVn-type systems.

An analogy with solar-type flares suggests that the WL flares in RS CVn-type systems are resulted from the process in which the particles accelerated in the magnetic reconnection bombard the upper photosphere. This scenario implies a violation of the Neupert effect in SVOM J00365+0033. The Neupert effect, being first revealed in solar flares by Neupert (1968), refers to a significant relationship between the thermal coronal emission and the time-integrated non-thermal emission, in which the heating due to the accelerated particles leads to a rapid expansion into the coronal loop, i.e., the so-called chromospheric evaporation, and a gradual cooling back to the quiescent state through thermal emission⁸ (e.g., Neupert 1968; Hudson & Ohki, 1972; Antonucci et al. 1984). As the evidence supporting the solar-stellar flare connection, the Neupert effect has been frequently reported in previous studies for the flares on RS CVn-type stars, main-sequence late-type stars and T Tauri stars (e.g., Hawley et al. 1995, 2003; Guedel et al. 1996; Gudel et al. 2002a, b, 2004; Osten et al. 2004; Mitra-Kraev et al. 2005; Audard et al. 2007; Wargelin et al. 2008; Fuhrmeister et al. 2011; Lalitha et al. 2013; Caballero-Gereia et al. 2015; Tristan et al. 2023), based on multi-wavelength observations.

In a stellar flare, its WL emission is commonly used as a proxy of the non-thermal hard X-ray ($\gg 10 \text{ keV}$) emission, both because of the difficulty in the detection of stellar hard X-ray emission and because the emission in the two bands is found to be closely correlated in the solar flares (e.g., Kleint et al. 2016). Compared to the soft X-ray emission ($< 20 \text{ keV}$), the non-thermal emission traced by the WL emission is delayed by ~ 50 minutes in SVOM J00365+0033.

Some notable exceptions to the Neupert effect have actually been identified not only in solar flares, but also in some stellar flares (e.g., Doyle et al. 1998; Ayres et al. 2001; Osten et al. 2005), although the underly-

⁸ The effect is commonly expressed as $F_{\text{SXR}} \propto \int F_{\text{HXR}}(t) dt$ or $dF_{\text{SXR}}/dt \propto F_{\text{HXR}}(t)$, where F_{SXR} and F_{HXR} are the soft and hard X-ray flaring fluxes, respectively.

ing physics causing the breakdown of the Neupert effect is still an open issue. Possible explanations include low ambient electron density (or EM), low efficiency of heating due to the high trapping efficiency, a deeper penetration of the photosphere resulting from more energetic particles and a transition region explosion with lower temperature (e.g., Ayres et al. 2001). However, the low EM (or electron density) scenario is unlikely to be supported by our estimation (see Sections 5.1 and 6.2).

The penetration length of the accelerated electrons is, however, an essential issue in applying the bombardment scenario to the WL flares in RS CVn-systems, although one could alternatively consider the role of beamed protons (e.g., Grinin & Sobolev 1989). The stopping length is predicted to be $h = 1.5 \times 10^{17} E^2 / n_e$ cm for an electron with an energy E in unit of keV (Brown 1971), where n_e is the electron density in unit of cm^{-3} . With the loop length (L) and n_e estimated above, the electrons with $E > 170$ keV are required to penetrate down to the photosphere.

Because of this difficulty, other two scenarios, thermal conduction and shock waves, have been proposed to interpret the origin of the WL flares in RS CVn-systems (e.g., Mullan 1976; Foing et al. 1994; Paudel et al. 2021). Although Foing et al. (1994) preferred the conduction scenario for the exceptional WL flares on HD 22468 detected in 1989, the X-ray to optical energy ratio is estimated to be ~ 0.1 in SVOM J00365+0033, which is inconsistent with the value of unit adopted in Mullan (1976).

7. CONCLUSIONS

The transient SVOM J00365+0033 is identified to be a superflare based on the associated WL flare and enhanced H α line emission. The light curve and spectral analysis in both hard X-ray and optical bands allow us to arrive at following conclusions:

1. The hard X-ray spectra of SVOM J00365+0033 can be well reproduced by the `apec` model with a high peak temperature of 106^{+27}_{-22} MK. The bolometric energy released in the event is estimated to be as high as $\sim 7.2 \times 10^{37} - 1.7 \times 10^{38}$ erg.
2. At ~ 1.7 hrs after the trigger, an upward plasma motion with respect to the photosphere is revealed by the bulk H α line blueshift at a velocity of -96 ± 20 km s $^{-1}$. This motion could be caused by either a chromospheric evaporation or a prominence eruption.

ACKNOWLEDGMENTS

We thank the anonymous referee for the helpful comments improving our study significantly. The Space-based multi-band astronomical Variable Objects Monitor (SVOM) is a joint Chinese-French mission led by the Chinese National Space Administration (CNSA), the French Space Agency (CNES), and the Chinese Academy of Sciences (CAS). We gratefully acknowledge the unwavering support of NSSC, IAMCAS, XIOPM, NAOC, IHEP, CNES, CEA, and CNRS. This study is supported by the National Key R&D Program of China (grant Nos. 2024YFA1611702, 2024YFA1611700), by the Strategic Pioneer Program on Space Science, Chinese Academy of Sciences, grant No. XDB0550401, and by the National Natural Science Foundation of China (grant Nos. 12494571, 12494570, 12494573). J.W. is supported by the National Natural Science Foundation of China (under grants 12173009). We acknowledge the support of the staff of the Xinglong 2.16m telescope and SVOM/GWAC. This work was partially supported by the Open Project Program of the Key Laboratory of Optical Astronomy, National Astronomical Observatories, Chinese Academy of Sciences.

Facilities: beijing: 2.16m

Software: IRAF (Tody 1986, 1992), MATPLOTLIB (Hunter 2007), Heasoft, Xspec (Arnaud 1996)

REFERENCES

Airapetian, V. S., Glocer, A., Gronoff, G., et al. 2016, *NatGe*, 9, 452

Airapetian, V. S., Glocer, A., Khazanov, G. V., Loyd, R. O. P., France, K., Sojka, J., Danchi, W. C., & Liemohn, M. W. 2017, *ApJL*, 836, 3

Antonucci, E., Gabriel, A. H., & Dennis, B. R. 1984, *ApJ*, 287, 917

Argiroff, C., Reale, F., Drake, J. J., et al. 2019, *Nature Astronomy*, 3, 742

Arnaud, K. A. 1996, Astronomical Data Analysis Software and Systems V, XSPEC: The First Ten Years, 101, 17

Atteia, J.-L., Cordier, B., & Wei, J. 2022, *International Journal of Modern Physics D*, 31, 2230008

Audard, M., Osten, R. A., Brown, A., et al. 2007, *A&A*, 471, 3, L6

Ayres, T. R., Brown, A., Osten, R. A., et al. 2001, *ApJ*, 549, 1, 554

Bai, J.-Y., Wang, J., Li, H. L., et al. 2023, *PASP*, 135, 064201

Balona, L. A. 2015, *MNRAS*, 447, 271

Berdyugina, S. V., Ilyin, I., & Tuominen, I. 1999, *A&A*, 349, 863

Bhatia, T. S., Cameron, R. H., Solanki, S. K., et al. 2023, *A&A*, 677, C1

Bohlin, R. C., Savage, B. D., & Drake, J. F. 1978, *ApJ*, 224, 132

Brosius, J. W. & Daw, A. N. 2015, *ApJ*, 810, 1, 45

Brosius, J. W., & Inglis, A. R. 2017, *ApJ*, 848, 39

Brown, J. C. 1971, *SoPh*, 18, 3, 489

Butler, C. J., Rodono, M., & Foing, B. H. 1988, *A&A*, 206, L1

Caballero-García, M. D., Šimon, V., Jelínek, M., et al. 2015, *MNRAS*, 452, 4, 4195

Canfield, R. C., Penn, M. J., Wulser, J., & Kiplinger, A. L. 1990, *ApJ*, 363, 318

Cao, D. & Gu, S. 2024, *ApJ*, 963, 13

Cao, D. & Gu, S. 2025, *AJ*, 169, 4, 198

Chang, H. -Y., Lin, C. -L., Ip, W. -H., Huang, L. -C., Hou, W. -C., Yu, P. -C., Song, Y. -H., & Luo, A. 2018, *ApJ*, 867, 78

Chen, B., Shen, C. Gary D. E., et al. 2020, *NatAs*, 4, 1140

Chen, G., Pallé, E., Parviainen, H., et al. 2021, *MNRAS*, 500, 4, 5420

Chen, H., Tian, H., Li, H., et al. 2022, *ApJ*, 933, 92

Cherenkov, A., Bisikalo, D., Fossati, L., & Mostl, C. 2017, *ApJ*, 846, 31

Davenport, J. R. A., Kipping, D. M., Sasselov, D., Matthews, J. M., & Cameron, C. 2016, *ApJL*, 829, 31

De Medeiros, J. R., Udry, S., & Mayor, M. 2004, *A&A*, 427, 313

Didel, S., Pandey, J. C., & Srivastava, A. K. 2025, *AJ*, 169, 1, 49

Doyle, J. G., Short, C. I., Byrne, P. B., et al. 1998, *A&A*, 329, 229

Emslie, A. G., Dennis, B. R., Shih, A. Y., et al. 2012, *ApJ*, 759, 71

Endl, M., Strassmeier, K. G., & Kurster, M. 1997, *A&A*, 328, 565

Evans, I. N., Primini, F. A., Glotfelty, K. J., et al. 2010, *ApJS*, 189, 1, 37

Fan, Z., Wang, H. J., Jiang, X. J., et al. 2016, *PASP*, 128, 5005

Feldman, U., Laming, J. M., & Doschek, G. A. 1995, *ApJL*, 451, L79

Fletcher, L., Dennis, B. R., Hudson, H. S., et al. 2011, *SSRv*, 159, 19

Fisher, G. H., Canfield, R. C., & McClymont, A. N. 1985, *ApJ*, 289, 414

Foing, B. H., Char, S., Ayres, T., et al. 1994, *A&A*, 292, 543

Franciosini, E., Pallavicini, R., & Tagliaferri, G. 2001, *A&A*, 375, 196

Fuhrmeister, B., Lalitha, S., Poppenhaeger, K., et al. 2011, *A&A*, 534, A133

Gaia Collaboration, Klioner, S. A., Lindegren, L., et al. 2022, *A&A*, 667, A148

Garcia-Sage, K., Glocer, A., Drake, J. J., Gronoff, G., & Cohen, O. 2017, *ApJL*, 844, 13

Getman, K. V. & Feigelson, E. D. 2021, *ApJ*, 916, 1, 32

Getman, K. V., Feigelson, E. D., & Garmire, G. P. 2023, *ApJ*, 952, 1, 63

Glebocki, R. & Gnacinski, P. 2005, *VizieR Online Data Catalog*, 3244. III/244

Godet, O., Nasser, G., Atteia, J., et al. 2014, *Proc. SPIE*, 9144, 9144424

Goldwurm, A. & Gros, A. 2022, *Handbook of X-ray and Gamma-ray Astrophysics*, 15.

Graham, D. R., Cauzzi, G., Zangrilli, L., Kowalski, A., Simoes, P., & Allred, J. 2020, *ApJ*, 895, 6

Grinin, V. P. & Sobolev, V. V. 1989, *Astrophysics*, 31, 3, 729

Güdel, M., Audard, M., Reale, F., et al. 2004, *A&A*, 416, 713.

Güdel, M., Audard, M., Skinner, S. L., et al. 2002a, *ApJL*, 580, 1, L73

Güdel, M., Audard, M., Smith, K. W., et al. 2002b, *ApJ*, 577, 1, 371

Guedel, M., Benz, A. O., Schmitt, J. H. M. M., et al. 1996, *ApJ*, 471, 1002

Gunn, A. G., Doyle, J. G., Mathioudakis, M., Houdebine, E. R., & Avgoloupis, S. 1994, *A&A*, 285, 489

Hakamata, T., Matsumoto, H., Odaka, H., et al. 2025, *PASJ*, 77, 2, 356

Han, X., Xiao, Y., Zhang, P., et al. 2021, *PASP*, 133, 065001

Hawley, S. L., Allred, J. C., Johns-Krull, C. M., et al. 2003, *ApJ*, 597, 1, 535

Hawley, S. L., Fisher, G. H., Simon, T., et al. 1995, *ApJ*, 453, 464

Heinzel, P., Gouttebroze, P., & Vial, J.-C. 1994, *A&A*, 292, 656

Herrero, E., Ribas, I., Jordi, C., et al. 2012, *A&A*, 537, A147

Honda, S., Notsu, Y., Namekata, K., et al. 2018, *PASJ*, 70, 4, 62

Hotta, H., Kusano, K., & Shimada, R. 2022, *ApJ*, 933, 199

Houdebine, E. R., & Doyle, J. G. 1994a, *A&A*, 289, 169

Houdebine, E. R., & Doyle, J. G. 1994b, *A&A*, 289, 185

Houdebine, E. R., Foing, B. H., & Rodono, M. 1990, *A&A*, 238, 249

Hudson, H. S. & Ohki, K. 1972, *SoPh*, 23, 1, 155

Huenemoerder, D. P., Schulz, N. S., Testa, P., Drake, J. J., Osten, R. A., & Reale, F. 2010, *ApJ*, 723, 1558

Hunter, J. D. 2007, *Computing in Science and Engineering*, 9, 90

Innes, D. E., Inhester, B., Axford, W. I., & Wilhelm, K. 1997, *Nature*, 386, 811

Inoue, S., Maehara, H., Notsu, Y., et al. 2023, *ApJ*, 948, 9

Inoue, S., Enoto, T., Namekata, K., et al. 2024, *PASJ*, 76, 175

Kamio, S., Kurokawa, H., Brooks, D. H., Kitai, R., & UeNo, S. 2005, *ApJ*, 625, 1027

Karmakar, S., Naik, S., Pandey, J. C., et al. 2023, *MNRAS*, 518, 1, 900

Kervella, P., Arenou, F., & Thévenin, F. 2022, *A&A*, 657, A7

Kleint, L., Heinzel, P., Judge, P., et al. 2016, *ApJ*, 816, 2, 88

Kurokawa, H., Hanaoka, Y., Shibata, K., et al. 1987, *SoPh*, 108, 251

Koller, F., Leitzinger, M., Temmer, M., Odert, P., Beck, P. G., & Veronig, A. 2021, *A&A*, 646, 34

Kowalski, A. F., Hawley, S. L., Wisniewski, J. P., Osten, R. A., Hilton, E. J., Holtzman, J. A., Schmidt, S. J., Davenport, J. R. A. 2013, *ApJS*, 207, 15

Kriss, G. 1994, in *ASP Conf. Ser.* 61, *Astronomical Data Analysis Software and Systems III*, ed. D. R. Crabtree, R. J. Hanisch, & J. Barnes (San Francisco, CA: ASP), 437

Lacombe, K., Pons, R., Amoros, C., et al. 2014, *Proc. SPIE*, 9144, 914451

Lalitha, S., Fuhrmeister, B., Wolter, U., et al. 2013, *A&A*, 560, A69

Le Provost, H., Schanne, S., Flouzat, C., et al. 2013, in *2013 IEEE Nuclear Science Symposium and Medical Imaging Conference (2013 NSS/MIC)*, 1

Leitzinger, M. & Odert, P. 2022, *Serbian Astronomical Journal*, 205, 1

Li, D., 2019, *RAA*, 19, 67

Li, D., Ning, Z. L., Huang, Y., & Zhang, Q. M. 2017, *ApJL*, 841, 9

Li, G. W., Wu, C., Zhou, G. P., et al. 2023a, *Research in Astronomy and Astrophysics*, 23, 015016

Li, G.-W., Wang, L., Yuan, H.-L., et al. 2024, *ApJ*, 971, 1, 114

Li, H. L., Wang, J., Xin, L. P., et al. 2023b, *ApJ*, 954, 142

Libbrecht, T., de la Cruz Rodriguez, J., Danilovic, S., Leenaarts, J., & Pazira, 2019, *A&A*, 621, L35

Linsky, J. L., Neff, J. E., Brown, A., et al. 1989, *A&A*, 211, 173

Llamas Lanza, M., Godet, O., Arcier, B., et al. 2024, *A&A*, 685, A163

Luck, R. E. 2017, *AJ*, 153, 1, 21

Maehara, H., Notsu, Y., Namekata, K., et al. 2021, *PASJ*, 73, 44

Maehara, H., Shibayama, T., Notsu, S., et al. 2012, *Nature*, 485, 478

Mao, X., Liu, H.-Y., Wang, S., et al. 2025, *ApJ*, 980, 2, 268

Massey, P., Strobel, K., Barnes, J. V., et al. 1988, *ApJ*, 328, 315

Milligan, R. O., Gallagher, P. T., Mathioudakis, M., Bloomfield, D. S., Keenan, F. P., & Schwartz, R. A. 2006, *ApJL*, 638, 117

Mitra-Kraev, U., Harra, L. K., Güdel, M., et al. 2005, *A&A*, 431, 679

Monet, D. G., Levine, S. E., Canzian, B., et al. 2003, *AJ*, 125, 2, 984

Moschou, S., Drake, J. J., Cohen, O., Alvarado-Gomez, J. D., Garraffo, C., & Fraschetti, F. 2019, *ApJ*, 877, 105

Mullan, D. J. 1976, *ApJ*, 207, 289

Namekata, K., Airapetian, V. S., Petit, P., et al. 2024, *ApJ*, 961, 23

Namekata, K., Maehara, H., Honda, S., et al. 2021, *NatAs*, 6, 241

Neupert, W. M. 1968, *ApJL*, 153, L59

Notsu, Y., Kowalski, A. F., Maehara, H., et al. 2024, *ApJ*, 961, 2, 189

Notsu, Y., Maehara, H., Shibayama, T., Honda, S., Notsu, S., Namekata, K., Nogami, D., & Shibata, K. 2016, The 19th Cambridge Workshop on Cool Stars, Stellar Systems, and the Sun (CS19), Uppsala, Sweden, 06-10 June 2016, id.119

Noyes, R. W., Hartmann, L. W., Baliunas, S. L., Duncan, D. K., & Vaughan, A. H. 1984, *ApJ*, 279, 763

Osten, R. A., Brown, A., Ayres, T. R., et al. 2004, *ApJS*, 153, 317

Osten, R. A., Drake, S., Tueller, J., et al. 2007, *ApJ*, 654, 2, 1052

Osten, R. A., Godet, O., Drake, S., et al. 2010, *ApJ*, 721, 1, 785

Osten, R. A., Hawley, S. L., Allred, J. C., Johns-Krull, C. M., & Roark, C. 2005, *ApJ*, 621, 398

Otsu, T., Asai, A., Ichimoto, K., et al. 2022, *ApJ*, 939, 2, 98

Pandey, J. C. & Singh, K. P. 2012, *MNRAS*, 419, 2, 1219

Paudel, R. R., Barclay, T., Schlieder, J. E., et al. 2021, *ApJ*, 922, 1, 31

Paudel, R. R., Gizis, J. E., Mullan, D. J., Schmidt, S. J., Burgasser, A. J., Williams, P. K. G., & Berger, E. 2018, *ApJ*, 858, 55

Pettersen, B. R. 1989, *A&A*, 209, 279

Pye, J. P., Rosen, S., Fyfe, D., et al. 2015, *A&A*, 581, A28

Rosen, S. R., Webb, N. A., Watson, M. G., et al. 2016, *A&A*, 590, A1

Sadykov, V. M., Vargas Dominguez, S., Kosovichev, A. G., Sharykin, I. N., Sturinsky, A. B., & Zimovets, I. 2015, *ApJ*, 805, 167

Sasaki, R., Tsuboi, Y., Iwakiri, W., et al. 2021, *ApJ*, 910, 1, 25

Schanne, S., Le Provost, H., Kestener, P., et al. 2013, in 2013 IEEE Nuclear Science Symposium and Medical Imaging Conference (2013 NSS/MIC), 1

Schmitt, J. H. M. M. 1994, *ApJS*, 90, 735

Schmidt, S. J., Shappee, B. J., van Saders, J. L., et al. 2019, *ApJ*, 876, 115

Seli, B., Oláh, K., Kriskovics, L., et al. 2022, *A&A*, 659, A3

Shibata, K. & Yokoyama, T. 2002, *ApJ*, 577, 1, 422

Shimizu, T. 1995, *PASJ*, 47, 251

Shulyak, D., Reiners, A., Engeln, A., Malo, L., Yadav, R., Morin, J., & Kochukhov, O. 2017, *Nature Astronomy*, 1, 184

Simon, T., Linsky, J. L., & Schiffer, F. H. 1980, *ApJ*, 239, 911

Smith, R. K., Brickhouse, N. S., Liedahl, D. A., et al. 2001, *ApJL*, 556, L91

Soubiran, C., Brouillet, N., & Casamiquela, L. 2022, *A&A*, 663, A4

Tan, B. L., Yan, Y., Li, T., et al. 2020, *RAA*, 20, 90

Tei, A., Sakaue, T., Okamoto, T. J., et al. 2018, *PASJ*, 70, 100

Teriaca, L., Falchi, A., Cauzzi, G., et al. 2003, *ApJ*, 588, 1, 596.

Tian, H., & Chen, N. H. 2018, *ApJ*, 856, 34

Tian, F., Kasting, J. F., & Zahnle, K. 2011, *E&PSL*, 308, 417

Tody, D. 1986, *Proc. SPIE*, 627, 733

Tody, D. 1993, in *ASP Conf. Ser.* 52, *Astronomical Data Analysis Software and Systems II*, ed. R. J. Hanisch, R. J. V. Brissenden, & J. Barnes (San Francisco, CA: ASP), 173

Tristan, I. I., Notsu, Y., Kowalski, A. F., et al. 2023, *ApJ*, 951, 1, 33

Tsuboi, Y., Yamazaki, K., Sugawara, Y., et al. 2016, *PASJ*, 68, 5, 90

Tsuru, T., Makishima, K., Ohashi, T., et al. 1989, *PASJ*, 41, 679

Van Doorsselaere, T., Shariati, H., & Debosscher, J. 2017, *ApJS*, 232, 26

Voges, W., Aschenbach, B., Boller, T., et al. 1999, *A&A*, 349, 389

Wang, J. 2023, *Research in Astronomy and Astrophysics*, 23, 095019

Wang, J., Xin, L. P., Li, H. L., et al. 2021, *ApJ*, 916, 92

Wang, J., Li, H. L., Xin, L. P., et al. 2022, *ApJ*, 934, 98

Wang, J., Mao, X., Gao, C., et al. 2024, *AJ*, 168, 6, 261

Wargelin, B. J., Kashyap, V. L., Drake, J. J., et al. 2008, *ApJ*, 676, 1, 610

Wei, J. Y., Cordier, B., Antier, S., et al. 2016, *arXiv:astro-ph/1610.0689*

Wiese, W. L., & Fuhr, J. R. 2009, *JPCRD*, 38, 565

Wu, Y., Chen, H., Tian, H., et al. 2022, *ApJ*, 928, 180

Wright, N. J., Drake, J. J., Mamajek, E. E., & Henry, G. W. 2011, *ApJ*, 743, 48

Xie, W., Cordier, B., Dagoneau, N., et al. 2024, *A&A*, 683, A60

Xin, L. P., Li, H. L., Wang, J., et al. 2021, *ApJ*, 909, 106

Xin, L. P., Li, H. L., Wang, J., et al. 2024, *MNRAS*, 527, 2232

Yan, X., Wang, J., Guo, Q., Xue, Z., Yang, L., & Tan, B. 2021, *ApJ*, 919, 34

Zhang, Q. M., Li, D., Ning, Z. J., Su, Y. N., Ji, H. S., & Guo, Y. 2016, *ApJ*, 827, 27